Bulletin of the Seismological Society of America, Vol. 106, No. 1, pp. –, February 2016, doi: 10.1785/0120150087

P-Wave Attenuation with Implications for Earthquake Early Warning

by Itzhak Lior, Alon Ziv, and Raul Madariaga

abstract
Abstract   Several widely implemented and tested earthquake early warning algorithms employ empirical equations that relate earthquake magnitudes with ground-motion peak amplitudes and hypocentral distances. This approach is effective to the extent that the offline dataset available for setting the fitting coefficients in those equations is of sufficient quality and quantity. However, to address the problem of having a limited dataset, it is instructive to gain physical understanding of the main factors controlling the *P*-wave attenuation. In this study, theoretical expressions are derived that relate the root mean square (rms) of the *P*-wave displacement d_{rms} and velocity v_{rms} to the seismic moment, stress drop, and hypocentral distance.

The theoretical attenuation laws are then validated against observed attenuation, using earthquake data from southern California and Japan. Good agreement is found between observed and predicted ground motions. The similar ground-motion attenuation in California and Japan suggests that the attenuation laws are similarly applicable for the two regions and implies that they may also be implemented in other regions without having to go through a lengthy calibration phase.

Because d_{rms} is more strongly dependent on the seismic moment than v_{rms}, use of the attenuation law for d_{rms} yields better magnitude prediction than that of v_{rms}. It is shown that the d_{rms}-to-v_{rms} ratio is proportional to the characteristic length of the rupture and that the stress drop is a function of the seismic moment and the cube of d_{rms}/v_{rms}. This result paves the way for a new stress-drop determination scheme that is totally independent of previously used approaches. Finally, it is shown that the rms of the ground motions are proportional to their peak values.

Introduction

Earthquake early warning systems (EEWS) run real-time algorithms that predict the shaking intensity and/or assess the alert level based on the first few seconds of the seismic record. Typically, these algorithms employ empirical relations that are obtained via regression analysis of offline earthquake records (e.g., Nakamura, 1984, 1988; Allen and Kanamori, 2003; Wu and Kanamori, 2005b; Cua and Heaton, 2007; Allen *et al.*, 2009; Böse *et al.*, 2009; Zollo *et al.*, 2009). One such relation is a *P*-wave attenuation law, describing how the *P*-wave peak velocity or displacement is related to earthquake magnitude and hypocentral distance. Owing to the site and source-specific characteristics affecting the ground motion, an attenuation law established for one tectonic setting may not be suitable for another. In addition, these relations suffer from strong trade-offs between different terms; and, unless the dataset is very large, inverting for the fitting coefficients is unstable. To address the problem of having a limited dataset and to facilitate the parameter tuning, when adjusting to different tectonic settings, it is instructive to gain physical understanding of the main factors controlling the *P*-wave attenuation.

In this study, theoretical expressions are derived that relate the root mean square (rms) of the *P*-wave ground motion (displacement and velocity) to the seismic moment, stress drop, and hypocentral distance. The theoretical attenuation laws are then validated against observed attenuation, using earthquake data from southern California and Japan. The use of displacement and velocity attenuation laws for real-time magnitude determination is discussed. Finally, it is shown that the ground-motion rms and peak values are linearly related.

Theoretical Attenuation Law

The rationale underlying this study is guided by the highly simplified view of earthquake ruptures as dynamic cracks that are embedded within a perfectly elastic medium (Madariaga, 1976). According to this view, the problem possesses an intrinsic length-scale, and the radiated wavefield is controlled primarily by the stress drop and the characteristic length-scale of the rupture. Thus, the attenuation law proposed below incorporates these parameters.

Displacement and Velocity Spectra

The far-field displacement spectra of *P* waves may be described by the omega-squared model

$$\Omega(\omega) = \frac{\Omega_0}{1 + (\frac{\omega}{\omega_0})^2} \tag{1}$$

(Aki, 1967; Brune, 1970), in which ω is the angular frequency, ω_0 is the angular corner frequency, and Ω_0 is the low-frequency spectral plateau. Similarly, the P-wave velocity spectra is described by

$$\dot{\Omega}(\omega) = \omega \frac{\Omega_0}{1 + (\frac{\omega}{\omega_0})^2}. \tag{2}$$

Thus, while the displacement spectral amplitude is flat below the corner frequency and decays as ω^{-2} above it, the velocity spectral amplitude is strongly peaked, with most energy being radiated at frequencies around the corner frequency. The angular corner frequency is related to the rupture dimensions as

$$\omega_0 = 2\pi f_0 = 2\pi \frac{kC_S}{r} \tag{3}$$

(Brune, 1970), in which f_0 is the corner frequency, r is the rupture radius, C_S is the shear-wave velocity, and k is a constant. The low-frequency spectral plateau is related to the seismic moment M_0 according to

$$\Omega_0 = \frac{M_0 U_{\varphi\theta} F_s}{4\pi\rho C_P^3 R}, \tag{4}$$

in which $U_{\varphi\theta}$ is the radiation pattern, F_s is a free-surface correction factor, C_P is the P-wave velocity, R is the hypocentral distance, and ρ is the density. For a penny-shaped crack, the seismic moment is related to the stress drop $\Delta\tau$ and the rupture radius as

$$M_0 = \frac{16}{7}\Delta\tau r^3 \tag{5}$$

(Eshelby, 1957). The anelastic and near-surface attenuations are not accounted for in equations (1) and (2). Indeed, for hypocentral distances relevant to EEW applications ($R < 60$ km from the source), the dissipation of P waves is weak and can be ignored (Wu *et al.*, 2005; Wu and Zhao, 2006). This will be checked in the next section. Near-surface effects, on the other hand, cannot be corrected for unless specific data about surface response were available, and they are considered here as part of the observational error.

Attenuation Law

Here, expressions are derived that relate the rms of the P-wave ground motion to the seismic moment, stress drop, and hypocentral distance. The rms of a given time series $y(t)$ may be calculated from its spectra $Y(f)$ using Parseval's theorem:

$$y_{\mathrm{rms}} = \sqrt{\frac{\int_{-\infty}^{\infty} |Y(f)|^2 df}{T_{S-P}}}, \tag{6}$$

in which T_{S-P} is the data interval that is set to be equal to the difference between the arrival times of the S and P waves, given by

$$T_{S-P} = R\left(\frac{1}{C_S} - \frac{1}{C_P}\right) \overset{\mathrm{def}}{=} R\eta. \tag{7}$$

Solving equation (6) using the displacement and velocity spectra in equations (1) and (2), respectively, yields displacement rms,

$$d_{\mathrm{rms}} = \Omega_0 \sqrt{\frac{\pi}{2}\frac{f_0}{T_{S-P}}}, \tag{8a}$$

and velocity rms,

$$v_{\mathrm{rms}} = 2\pi\Omega_0 \sqrt{\frac{\pi}{2}\frac{f_0^3}{T_{S-P}}}. \tag{8b}$$

By substituting equations (3)–(5) and (7) into equations (8a) and (8b), the attenuation of d_{rms}; and v_{rms} may be either expressed in terms of stress drop and seismic moment:

$$d_{\mathrm{rms}} = \epsilon\left(\frac{16}{7}\Delta\tau\right)^{1/6} M_0^{5/6} \frac{1}{R^{3/2}} \tag{9a}$$

and

$$v_{\mathrm{rms}} = \epsilon\left(\frac{16}{7}\Delta\tau\right)^{1/2} M_0^{1/2} 2\pi kC_S \frac{1}{R^{3/2}}, \tag{9b}$$

or it may be expressed in terms of the stress drop and the rupture length-scale as

$$d_{\mathrm{rms}} = \epsilon \frac{16}{7}\Delta\tau\left(\frac{r^{5/3}}{R}\right)^{3/2} \tag{10a}$$

and

$$v_{\mathrm{rms}} = \epsilon \frac{16}{7}\Delta\tau 2\pi kC_S\left(\frac{r}{R}\right)^{3/2}, \tag{10b}$$

with ϵ being a constant that collects all the parameters that are in common to equations (9) and (10):

$$\epsilon = \frac{U_{\varphi\theta} F_s}{4\pi\rho C_P^3} \sqrt{\frac{\pi kC_S}{2\eta}}. \tag{11}$$

Statistical theories and models predict a direct relation between the rms and the absolute extremum of a given time series (Cartwright and Longuet-Higgins, 1956; Davenport, 1964; Clough and Penzien, 1975). Thus, in principle, the peak and the rms of the ground vibrations attenuate similarly. This conjecture has already been exploited in the past by several seismologists in the context of ground-motion prediction (Hanks and McGuire, 1981; Boore, 1983, 2003; Boore and Joyner, 1984). Later it is verified empirically that v_{rms} and d_{rms} are indeed proportional to the peak velocity P_v and peak displacement P_d, which are in use by several EEW algorithms (e.g., Wu and Kanamori, 2005b; Cua and Heaton, 2007; Lan-

cieri and Zollo, 2008; Böse *et al.*, 2009; Zollo *et al.*, 2009; Brown *et al.*, 2011; Lancieri *et al.*, 2011; Sadeh *et al.*, 2013).

Theory Versus Observations

In this section, theoretical attenuation laws are validated against observed attenuation using earthquake data from southern California and Japan. Throughout this article, the following parameter settings are used: $U_{\phi\theta} = 0.52$, $F_s = 2$, $\rho = 2600$ kg/m^3, $C_S = 3200$ m/s, $C_P = 5333$ m/s, and $k = 0.32$ (Madariaga, 1976), and the seismic moments are obtained from the catalog magnitude using the moment-magnitude relation of Hanks and Kanamori (1979). With the above parameter settings, η and ϵ are equal to $\frac{1}{8}$ s/km and 7.5×10^{-13} 1/Pa, respectively. One last parameter that enters the problem is the stress drop, the value of which is set to be equal to the median stress drop. Simple schemes for inferring the stress drop are described in the Stress-Drop Assessment section.

Data

A composite dataset is used that consists of 403 velocity seismograms recorded by the broadband seismometers of the California Integrated Seismic Network and 353 accelerograms recorded by the K-NET and KiK-net surface accelerometers (Fig. 1). These data are associated with 120 southern California earthquakes with magnitudes between 4 and 5.7 and 42 Japanese earthquakes with magnitudes between 5.1 and 7.3. Hypocentral distances are limited to 60 km (Fig. 2). Raw data were inspected visually for quality control, *P*-wave arrivals were picked manually, and zero-offset corrections were applied. Three-component displacement and velocity time series were obtained via integration of the seismic records, with starting times and interval lengths that were set to the time of the first *P* arrivals and 90% of the T_{S-P} intervals, respectively. The latter were set to 1 s per 8 km of hypocentral distance, and the 10% shortening ensures that the signal is not contaminated by *S*-wave energy. Using this practice and given that the largest hypocentral distance considered in this study is 60 km long, the longest data intervals are about 6.75 s long (but the average is much shorter). Because the data intervals are so short, the errors introduced by the single or double time-integration of low-frequency noise are small. The parameters $d_{\rm rms}$ and $v_{\rm rms}$ were calculated according to $\sqrt{\sum_{i=1}^{n}[AZ_i^2 + AE_i^2 + AN_i^2]/n}$, in which n is the number of samples within the data interval and AZ_i, AE_i, and AN_i are the velocity or displacement amplitudes along the vertical, east, and north directions, respectively. A comparison between raw and high-pass-filtered $d_{\rm rms}$ reveals that high-pass filtering the displacement seismograms introduces a magnitude bias, such that the amplitudes of the moderate-big Japanese earthquakes (circles in Fig. 3) are more reduced than those of the small California earthquakes (triangles in Fig. 3). For this reason, and keeping in mind that the data intervals end before the arrival of *S* waves (therefore sensor
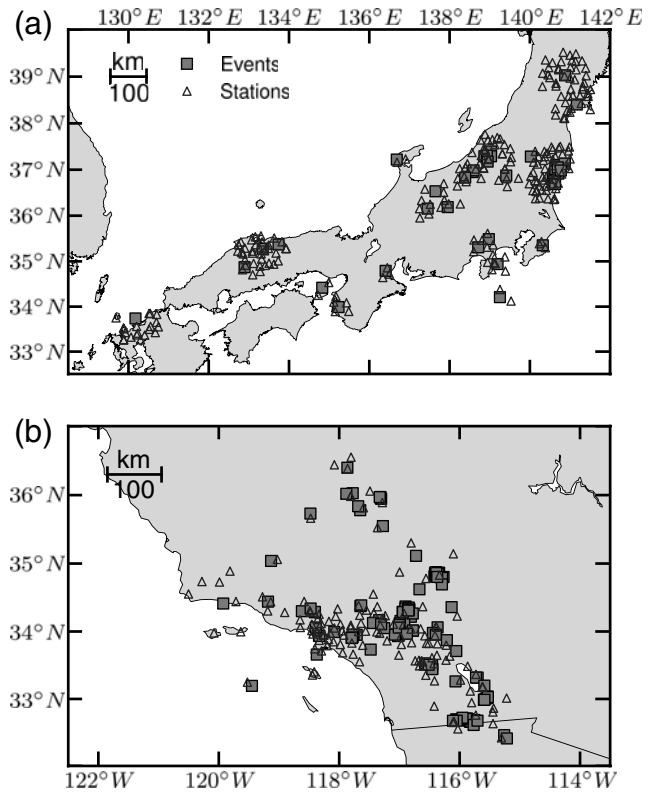

Figure 1. Location map showing earthquakes (squares) and stations (triangles) in (a) Japan and (b) southern California.

tilt is unlikely), it was decided not to follow the common practice of high-pass filtering the displacement seismograms, including those that were obtained via double integration of acceleration time series. Signal-to-noise ratios (SNRs) were assessed using

$$\text{SNR} \overset{\text{def}}{=} \sqrt{\frac{\sum_{i=1}^{l} AZ_i^2}{l}} \Bigg/ \sqrt{\frac{\sum_{j=1}^{m} AZ_j^2}{m}}, \qquad (12)$$

with AZ_i being the raw vertical ground motion (velocity or acceleration), and l and m are the number of samples within the data and the presignal intervals, respectively, with the latter extending up to 20 s. Records with SNR smaller than 20 were excluded from the dataset.

Stress-Drop Assessment

The newly derived attenuation laws for $d_{\rm rms}$ and $v_{\rm rms}$ are now used to derive expressions for the stress drop. Dividing attenuation laws (9b) by (9a) and solving for the stress drop yields (Andrews, 1986; Snoke, 1987)

$$\Delta\tau = \frac{7}{16} M_0 \left(\frac{1}{2\pi k C_S} \frac{v_{\rm rms}}{d_{\rm rms}} \right)^3. \qquad (13)$$

An important aspect of this expression is that the term inside the parenthesis is the inverse of the characteristic length of the rupture r. Later it is demonstrated that this equation is
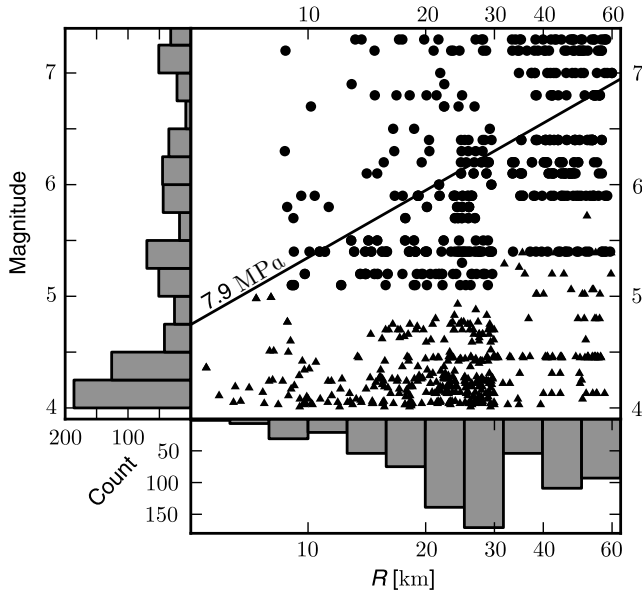
Figure 2. Waveform distribution according to magnitude and hypocentral distances. Triangles indicate broadband velocity data recorded by the California Integrated Seismic Network, and circles indicate accelerograms recorded by the K-NET and KiK-net surface accelerometers. The condition that the data interval be larger than the rupture duration is satisfied below the solid line of 7.9 MPa stress drop.

Figure 3. A comparison between raw and high-pass-filtered d_{rms}. Log–log diagram showing d_{rms} high-pass filtered at 0.02 Hz as a function of raw d_{rms}. Triangles indicate broadband velocity data recorded by the California Integrated Seismic Network, and circles indicate accelerograms recorded by the K-NET and KiK-net surface accelerometers. The dashed and solid green lines are the 1:1 and the linear best fit, respectively. The fitting coefficients and the standard deviation of the linear fit are reported at the bottom right corner. Colors indicate magnitude bins.

closely related to τ_c, a frequency-based magnitude proxy that is widely used by EEWS (Wu and Kanamori, 2005a). A different expression for the stress drop may be obtained via substitution of M_0 in equation (13) into (9a):

$$\Delta\tau = \frac{v_{rms}^{2.5}}{d_{rms}^{1.5}} \frac{R^{1.5}}{\epsilon^{\frac{16}{7}} (2\pi k C_S)^{2.5}}. \quad (14)$$

In both expressions, the stress drop is a function of v_{rms}, d_{rms}, and C_S; however, while in equation (13) it is also a function of the seismic moment, in equation (14) it is a function of ϵ and the hypocentral distance. Thus, the obvious advantage of equation (13) with respect to equation (14) is that it is independent of ϵ. Use of equation (14) may be advantageous in areas where ϵ is well constrained, because the distance uncertainties are much smaller than those of the seismic moment.

Equations (13) and (14) pave the way for new stress-drop determination schemes that are totally independent of previously used approaches utilizing the far-field ground-motion spectra. However, because earthquake source parameters may not be reliably estimated using data intervals that are much shorter than the rupture duration, the above expressions cannot be used indiscriminately for the entire dataset. To screen out data points corresponding to rupture durations that may be longer than the data interval, the rupture duration of each earthquake was estimated based on the ratio of the rupture diameter and the rupture speed, with the latter being set to $0.9C_S$:
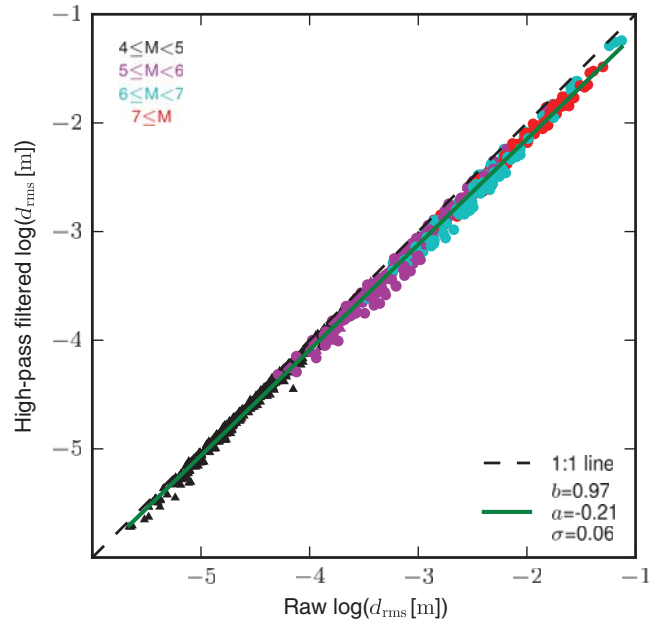
$$T_r = \frac{2r}{0.9C_S}. \quad (15)$$

In estimating the rupture diameter, a strict approach of overestimating the rupture duration at the price of screening out some good data points is sought. Thus, rupture diameters were estimated using equation (5), employing a relatively small stress drop of 1 MPa. About 67% of the seismograms analyzed in this study satisfy the condition that $T_{S-P} > T_r$. For this subset of seismograms, stress drops were calculated using equations (13) and (14). Stress drops as a function of catalog magnitude are shown in Figure 4 for individual data points (triangles and circles indicate California and Japanese earthquakes, respectively) and event averages (× symbols), with the latter reported only for a subset of events for which four or more seismograms are available. The median stress drops are detailed in Figure 4. These values are in good agreement with previous stress-drop estimates that use totally different methodologies (e.g., Hanks and Thatcher, 1972; Mayeda and Walter, 1996; Oth et al., 2010; Baltay et al., 2011, 2013; Abercrombie, 2013). In the next section, theoretical attenuation curves are calculated using a stress drop that corresponds to the median value of the individual data points (7.9 MPa) and a characteristic rupture dimension that is obtained through substitution of this stress-drop estimate into equation (5).

Observed Attenuation

Observed and predicted v_{rms} and d_{rms} are compared in Figures 5 and 6, with data points corresponding to rupture
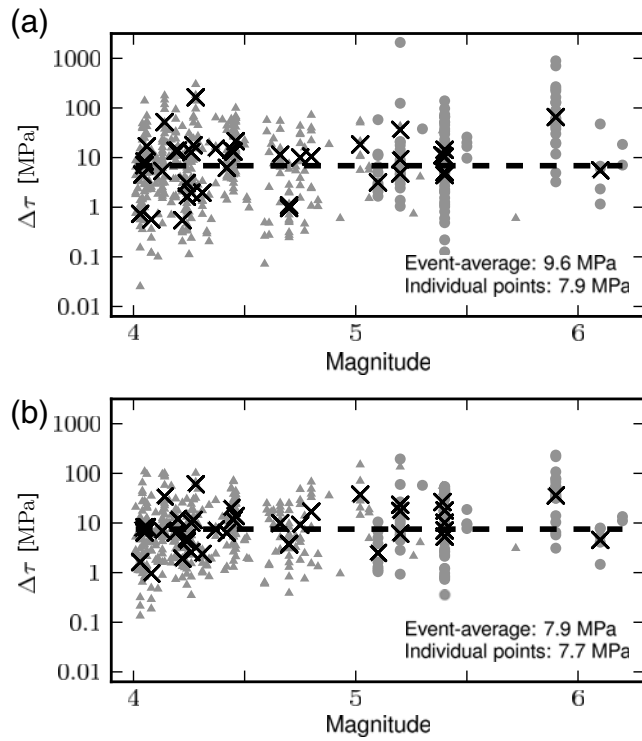
Figure 4. Stress-drop estimates using: (a) equation (13) and (b) equation (14) as a function of catalog magnitude. Single-station estimates for California and Japan are indicated by triangles and circles, respectively. Event-averaged estimates, for a subset of events for which four or more seismograms are available, are indicated by × symbols. Medians for event averages and for single data points are detailed in the legends. The dashed lines indicate the medians of the single-station estimates. Excluded from this diagram are data points for which $T_{S-P} < T_r$, in which T_r is defined in equation (15).

durations that are longer and shorter than T_{S-P} indicated by open and filled symbols, respectively. The rupture duration is estimated using the 7.9 MPa stress drop obtained in the previous section using equation (13), data points for which the rupture duration is shorter than T_{S-P} plot below the solid line labeled 7.9 MPa on the magnitude versus log-of-distance diagram in Figure 2. In Figure 5, v_{rms} and d_{rms} are plotted as a function of the hypocentral distance, and the theoretical curves are those of equations (9a) and (9b); in Figure 6, v_{rms} and d_{rms} are plotted as a function of R/r and $R/r^{5/3}$, respectively, and the theoretical curves are those of equations (10a) and (10b). The effect of dividing the distance axes by the source radius is to collapse the highly scattered cloud of data points in Figure 5 onto a narrow band that is highly centered about the theoretical curves (blue dashed lines) in Figure 6. Not surprisingly, the subset of data points that plot significantly below the theoretical lines are those for which the rupture duration is much longer than the T_{S-P} interval (open symbols in Figs. 5 and 6). To further assess the agreement between theory and observations, the data in Figure 6a were fit using

$$\log_{10}(d_{rms}) = a_d + b_d \log_{10}(R/r^{5/3}), \qquad (16a)$$

and those in Figure 6b were fit using

$$\log_{10}(v_{rms}) = a_v + b_v \log_{10}(R/r), \qquad (16b)$$

with a_d, b_d, a_v, and b_v being the fitting coefficients, the values of which are reported in the legends of Figure 6. The above attenuation laws can only be expected to be valid if anelastic attenuation is unimportant and when the data interval is not much shorter than the rupture duration. To guarantee that the latter condition is met, data points plotted above the 7.9 MPa line in Figure 2 (indicated by the open symbols in Figs. 5 and 6) were excluded from the linear fits in Figure 6. Best-fitting curves for $R < 30$ km and $R < 60$ km are shown in red and green, respectively (Fig. 6). Similarly, good agreement is found between best-fitting curves of different distance ranges and the theoretical curves. It is concluded that the neglect of the anelastic attenuation in equations (1) and (2) is justified, and the theoretical attenuation laws are valid for distances of up to at least 60 km, provided that T_{S-P} is longer than the rupture duration. The observation that many of the open symbols plot below the theoretical line in Figure 6 strongly implies that the final size of the source cannot be estimated using data intervals that are much shorter than the rupture duration.

The attenuations in Japan and California are examined separately and are compared to the theoretical attenuation in Figure 7. The similar ground-motion attenuation in California and Japan suggests that the attenuation laws are similarly applicable for the two regions and implies that they may also be implemented in other regions with similar tectonic setting. The integration of the newly obtained attenuation laws into EEW algorithms is most advantageous in places where the use of offline data for parameter tuning is limited by their quality and/or quantity.

Implications for EEW

Real-Time Magnitude Determination

The performances of three independent magnitude estimates are assessed. The first two expressions are obtained by solving the theoretical attenuation laws (equation 9) for the seismic moment:

$$M_0 = \frac{d_{rms}^{1.2} R^{1.8}}{(\frac{16}{7}\Delta\tau)^{0.2}\epsilon^{1.2}} \qquad (17a)$$

and

$$M_0 = \frac{v_{rms}^2 R^3}{\frac{16}{7}\Delta\tau 2\pi k C_S \epsilon^2}. \qquad (17b)$$

A third expression is obtained by inserting equation (13) into (9a) and solving for the seismic moment:

$$M_0 = \frac{d_{rms}^{1.5}}{v_{rms}^{0.5}}\frac{(2\pi k C_S)^{0.5} R^{1.5}}{\epsilon}. \qquad (18)$$
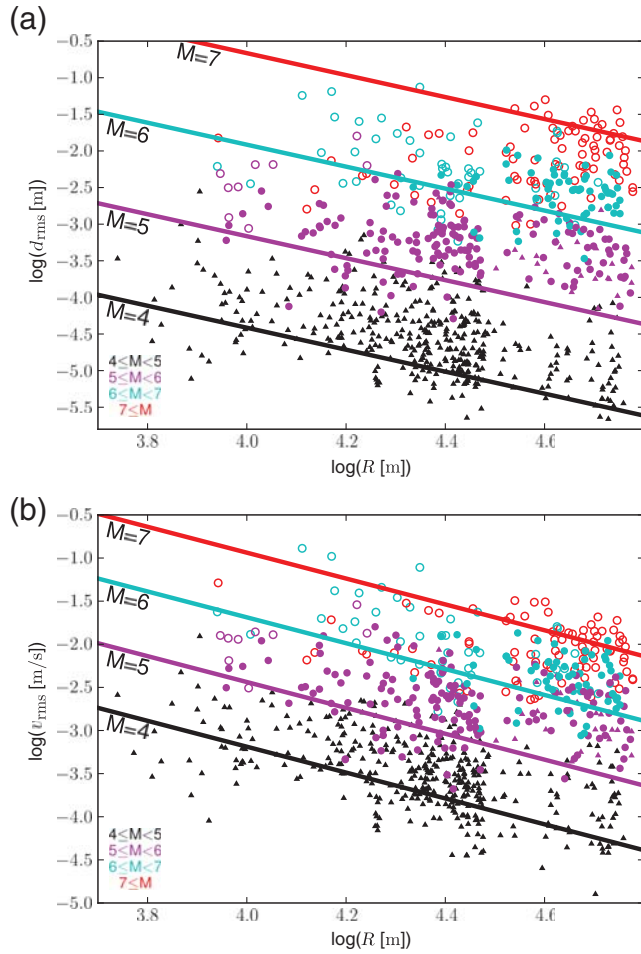
Figure 5. Root mean square (rms) of (a) the ground-motion displacement and (b) velocity as a function of the hypocentral distance. Rupture durations that are longer than T_{S-P} are indicated by open symbols, and those shorter than T_{S-P} are indicated by solid symbols. Data from California and Japan are indicated by triangles and circles, respectively. Colors represent magnitude bins. Solid lines are theoretical curves corresponding to equations (9a) and (9b).

Figure 6. The rms of (a) the ground-motion displacement and (b) velocity as a function of $R/r^{5/3}$ and R/r, respectively. Rupture durations that are longer than T_{S-P} are indicated by open symbols, and those shorter than T_{S-P} are indicated by solid symbols. Data from California and Japan are indicated by triangles and circles, respectively. Colors represent magnitude bins. Blue dashed lines are theoretical curves corresponding to equations (10a) and (10b). Linear fits for $R \leq 30$ km and $R \leq 60$ km are indicated by red and green lines, respectively. Fitting coefficients in equations (16a) and (16b), and standard deviations are reported at the bottom-left corner of each panel.

Although equations (17a) and (17b) are a function of some *a priori* stress-drop value, equation (18) is not. In this study, equations (17a) and (17b) are solved by setting the stress drop to be equal to the median value of 7.9 MPa, reported in the previous section. The statistics of the predicted versus observed magnitude discrepancies are presented in Figure 8. Reasonably good agreement is found between predicted and observed earthquake magnitudes in cases where the data intervals are longer than the rupture durations. However, when this is not the case the predicted magnitudes typically fall below the observed values. Furthermore, use of equations (17a) and (18) yields better magnitude prediction than that of equation (17b). This result is attributed to d_{rms} being more strongly dependent on the seismic moment than v_{rms}, that is, $d_{rms} \propto M_0^{5/6}$ versus $v_{rms} \propto M_0^{1/2}$ in equations (9a) and (9b).

The accuracy of real-time magnitude determination schemes utilizing *P*-wave attenuation laws is subject to the accuracy of the real-time hypocentral distance. Inspection of
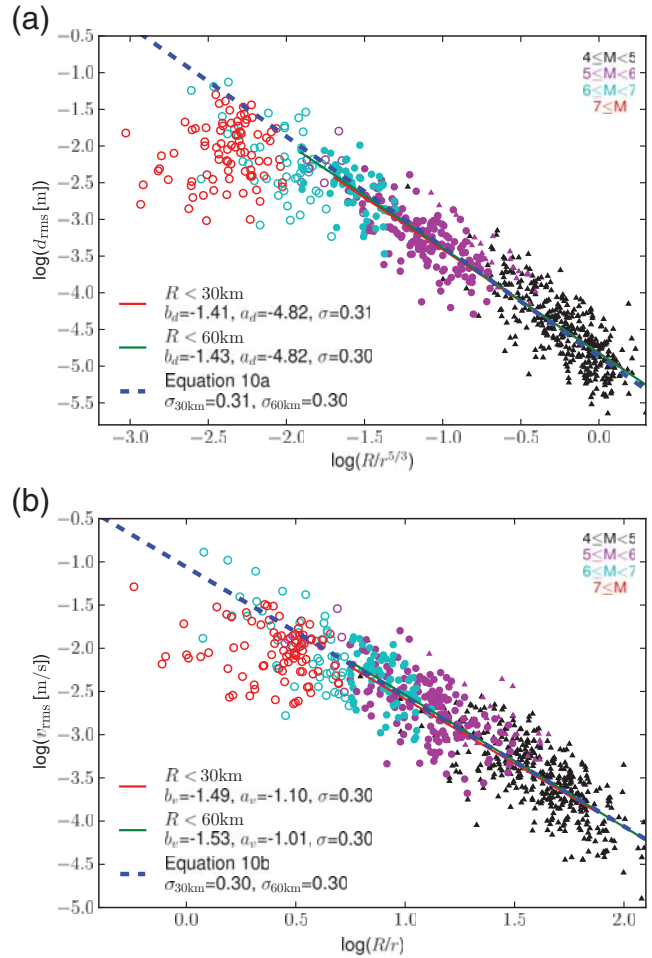
equations (17) and (18) reveals stronger distance sensitivity in equation (17b) than in equations (17a) and (18). Nevertheless, thanks to the logarithmic nature of the moment-magnitude relation and the accuracy of available real-time distance determination schemes (e.g., Satriano *et al.*, 2008; Kurzon *et al.*, 2014; Eisermann *et al.*, 2015), it is expected that magnitude estimates employing these equations will not be dramatically affected by the distance inaccuracies.

From v_{rms} and d_{rms} to P_v and P_d

Currently implemented network-based EEW algorithms employ empirical attenuation laws for the *P*-wave peak displacement P_d and/or peak velocity P_v (Cua and Heaton,
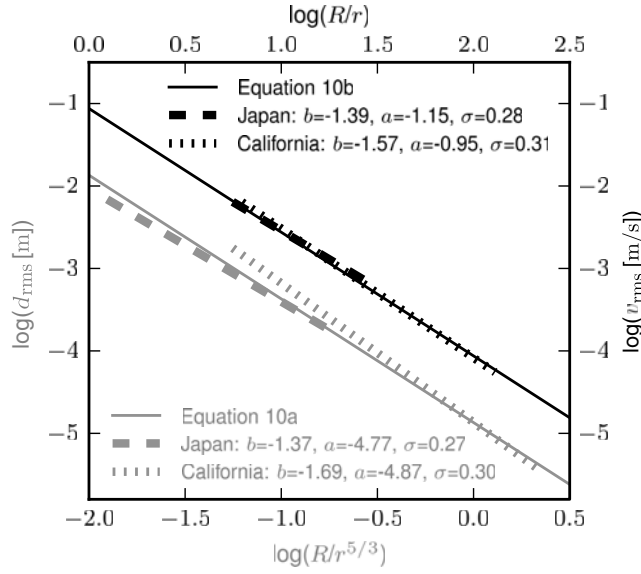
Figure 7. Comparison between ground-motion attenuation in California (dotted) and Japan (dashed). Gray lines are linear best fits to $\log(d_{rms})$ versus $\log(R/r^{5/3})$ (left and bottom axes), and black lines are linear best fits to $\log(v_{rms})$ versus $\log(R/r)$ (right and top axes). Solid gray and solid black lines are theoretical curves corresponding to equations (10a) and (10b), respectively. Fits were computed using data satisfying $T_{S-P} > T_r$. The best-fitting coefficients are detailed.

2007; Lancieri and Zollo, 2008; Zollo *et al.*, 2009; Brown *et al.*, 2011; Doi, 2011). It is thus instructive to see how these parameters are related to d_{rms} and v_{rms}. Log–log diagrams of P_d as a function of d_{rms} and P_v as a function of v_{rms} are shown in Figure 9, with peak displacement and peak velocity calculated according to $\max(\sqrt{AZ_i^2 + AE_i^2 + AN_i^2})$, in which i is the index of the data sample and AZ_i, AE_i, and AN_i are the velocity or displacement amplitudes along the vertical, east, and north directions, respectively. Inspection of these diagrams reveals excellent correlation between the peak and the rms of the ground motions. Regression analyses yield ~1 slopes on the log–log diagrams of Figure 9, thus indicating linear relations between the peak and the rms of the P-wave vibrations, with a similar constant of proportionality for displacement and velocity:

$$P_d = 2.0(\pm 0.5)d_{rms} \qquad (19a)$$

and

$$P_v = 2.3(\pm 0.5)v_{rms}. \qquad (19b)$$

These empirical relations are consistent with statistical theories and models (Cartwright and Longuet-Higgins, 1956; Davenport, 1964; Clough and Penzien, 1975) that were previously used in the context of ground-motion prediction equations (Hanks and McGuire, 1981; Boore, 1983, 2003; Boore and Joyner, 1984). The similarly excellent fit of data from California and Japan to the regression curves implies

that the above peak-versus-rms relations are nearly independent of site conditions and geological setting. One may now substitute the above empirical relations into equations (9a) and (9b) or (10a) and (10b) to obtain semiempirical attenuation laws for P_d and P_v.

Theoretical τ_c

The characteristic period of the signal's first few seconds τ_c is a frequency-based real-time magnitude proxy, which together with P_d, forms the basis for the $P_d-\tau_c$ onsite EEWS (Kanamori, 2005; Wu and Kanamori, 2005a,b). An interesting by-product of this study is revealed by noting that τ_c is proportional to the d_{rms} to v_{rms} ratio:

$$\tau_c = 2\pi \sqrt{\frac{\int_{t_0}^{t_0+\Delta t} u^2 dt}{\int_{t_0}^{t_0+\Delta t} v^2 dt}} = 2\pi \frac{d_{rms}}{v_{rms}}, \qquad (20)$$

in which u and v are the ground displacement and velocity, respectively, t_0 is the first P-wave arrival, and Δt is a prespecified interval. Dividing attenuation laws (8a) by (8b) indicates that τ_c is equal to the reciprocal of the corner frequency, thus explaining why it may be used as a proxy for the earthquake size. Substituting the above expression into equation (13) yields a theoretical expression for τ_c:

$$\tau_c = \frac{1}{kC_S} \sqrt[3]{\frac{7}{16} \frac{M_0}{\Delta\tau}}. \qquad (21)$$

Theoretical and observed τ_c are compared in Figure 10. Despite the large data scatter and the poor agreement between observed and theoretical τ_c, the correlation between the logarithm of τ_c and the catalog magnitude is statistically meaningful. Recently, Ziv (2014) has introduced τ_{log}, a frequency-based real-time magnitude proxy that is obtained by averaging the logarithm of the velocity spectra and has shown that its correlation with earthquake magnitude is significantly better than that of τ_c.

Conclusions

Two equivalent attenuation laws are presented for the rms of the P-wave velocity and displacement; in both, v_{rms} and d_{rms} are a function of the stress drop and the hypocentral distance; however, in one they are also a function of the seismic moment, but in the other they are a function of the characteristic rupture length. In deriving these relations, the data interval is set to be equal to the difference between the arrival times of the S and P phases. Furthermore, it is assumed that the ground-motion spectra obey the omega-squared model and that anelastic attenuation is unimportant. It is shown that $d_{rms} \propto \Delta\tau^{1/6} M_0^{5/6} R^{-3/2} \propto \Delta\tau \times r^{5/6} R^{-3/2}$ and $v_{rms} \propto \Delta\tau^{1/2} M_0^{1/2} R^{-3/2} \propto \Delta\tau \times r^{3/2} R^{-3/2}$ (equations 9a–10b).
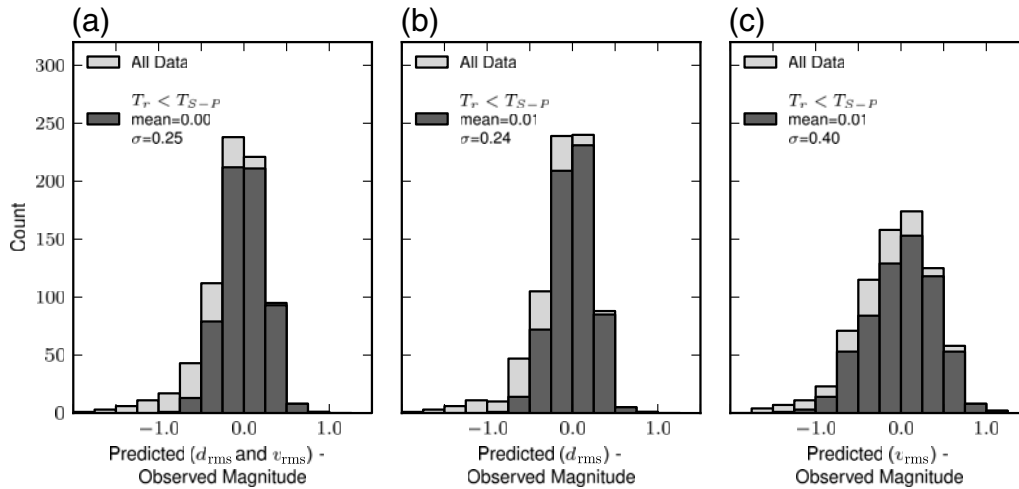
Figure 8. The distribution of the discrepancies between predicted and observed magnitude. Predicted magnitudes are calculated using the stress-drop-independent equation (17) and (18), setting the stress drop in those equations to be equal to the median value reported in Figure 4 (7.9 MPa). (a) Magnitudes are obtained using equation (18) for d_{rms} and v_{rms}. (b) Magnitudes are obtained using equation (17a) for d_{rms}. (c) Magnitudes are obtained using equation (17b) for v_{rms}. Light columns indicate the entire dataset, and dark columns indicate a subset of the data, for which the data intervals are longer than the rupture duration, that is, $T_{S-P} > T_r$. The mean and standard deviation of the magnitude discrepancies, corresponding to the data intervals that are longer than the rupture durations, are reported on each panel.
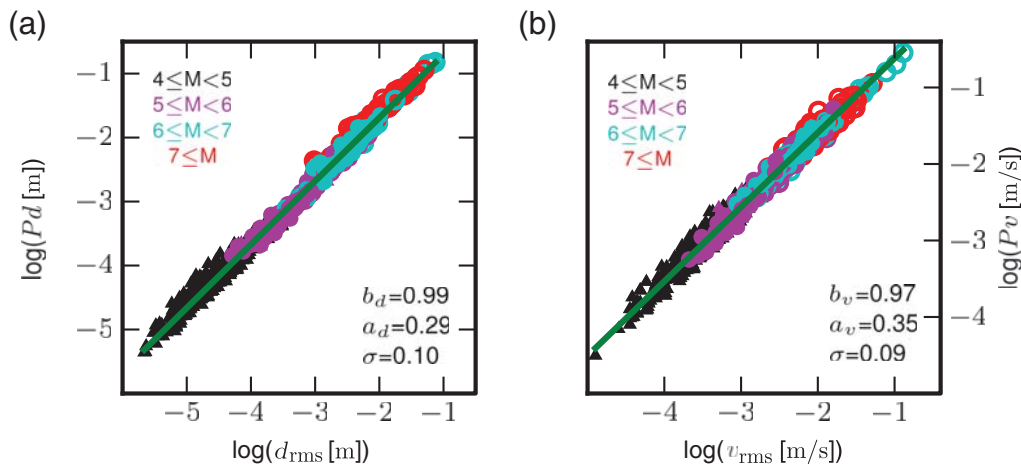

Figure 9. Log–log diagrams showing the peak ground motion as a function of the ground-motion rms. (a) $\log(P_d)$ versus $\log(d_{rms})$. (b) $\log(P_v)$ versus $\log(v_{rms})$. Green lines indicate least-square fits to $\log(d_{rms}) = a_d + b_d \times \log(P_d)$ and $\log(v_{rms}) = a_v + b_v \times \log(P_v)$, with fitting coefficients and standard deviations reported at the bottom-right corner of each panel. Data from California and Japan are indicated by triangles and circles, respectively. Colors represent magnitude bins.

Theoretical attenuation laws are validated against local earthquakes from Japan and California. Similarly good agreement between observed and predicted ground motion is found for hypocentral distances up to 30 and 60 km. It is thus concluded that the neglect of anelastic effects at these distance ranges is justified. It is shown that the v_{rms}-to-d_{rms} ratio is proportional to the characteristic length of the rupture and that the stress drop is a function of the seismic moment and the cube of d_{rms}/v_{rms} (equation 13). Using this result, a median stress drop of 7.9 MPa is obtained.

To assess the potential of these results for EEW applications, earthquake magnitudes are estimated using theoretical attenuation laws (9a) and (9b), either by setting the stress drop in those equations to be equal to the median value or by replacing equation (13) into (9a). Good agreement is found between predicted and observed earthquake magnitudes in cases in which the data intervals are longer than the rupture durations. However, when this is not the case, the predicted magnitudes fall below the observed values. Because d_{rms} is more strongly dependent on the seismic moment than v_{rms}, the use of equations (17a) and (18) yield better magnitude prediction than that of equation (17b).

Data and Resources

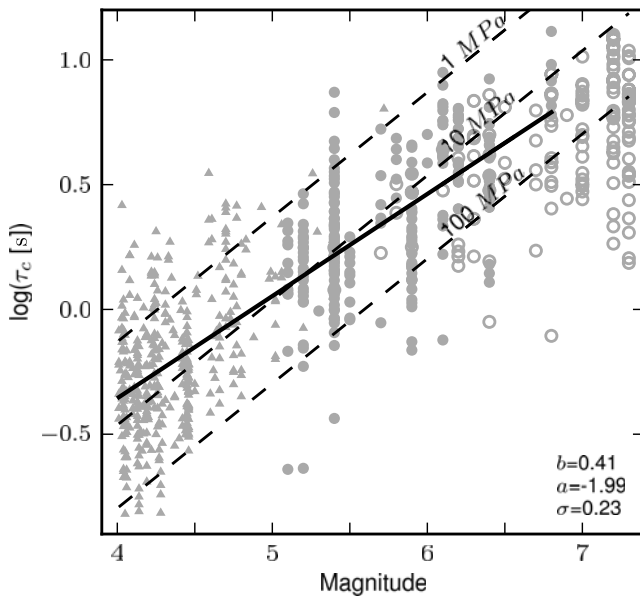The data used in this study were obtained from the Southern California Earthquake Data Center (http://scedc.caltech.

Figure 10. Characteristic period τ_c as a function of catalog magnitude. Triangles and circles indicate data from California and Japan, respectively. Theoretical lines corresponding to different stress drops are calculated using equation (21). Rupture durations that are longer and shorter than the data intervals T_{S-P} are indicated by open and filled symbols, respectively. Thick line indicates least-square fit of the filled symbols to $\log(\tau_c) = a + b \times M$, where M is the catalog magnitude, fitting coefficients, and standard deviation are reported at the bottom-right corner.

edu/, last accessed January 2015) and from the K-NET and KiK-net strong-motion networks (http://www.kyoshin.bosai. go.jp/, last accessed January 2015).

Acknowledgments

References

Abercrombie, R. E. (2013). Comparison of direct and coda wave stress drop measurements for the Wells, Nevada, earthquake sequence, *J. Geophys. Res.* **118,** 1458–1470.

Aki, K. (1967). Scaling law of seismic spectrum, *J. Geophys. Res.* **72,** 1217–1231.

Allen, R. M., and H. Kanamori (2003). The potential for earthquake early warning in southern California, *Science* **300,** 786–789.

Allen, R. M., H. Brown, M. Hellweg, O. Khainovski, P. Lombard, and D. Neuhauser (2009). Real-time earthquake detection and hazard assessment by ElarmS across California, *Geophys. Res. Lett.* **36,** L00B08, doi: 10.1029/2008GL036766.

Andrews, D. J. (1986). Objective determination of source parameters and similarity of earthquakes of different size, in *Earthquake Source Mechanics*, S. Das, J. Boatwright, and C. H. Scholz (Editors), American Geophysical Union, Washington, D.C., 259–268.

Baltay, A. S., T. C. Hanks, and G. C. Beroza (2013). Stable stress-drop measurements and their variability: Implications for ground-motion prediction, *Bull. Seismol. Soc. Am.* **103,** 211–222.

Baltay, A., S. Ide, G. Prieto, and G. Beroza (2011). Variability in earthquake stress drop and apparent stress, *Geophys. Res. Lett.* **38,** L06303, doi: 10.1029/2011GL046698.

Boore, D. M. (1983). Stochastic simulation of high-frequency ground motions based on seismological models of the radiated spectra, *Bull. Seismol. Soc. Am.* **73,** 1865–1894.

Boore, D. M. (2003). Simulation of ground motion using the stochastic method, *Pure Appl. Geophys.* **160,** 635–676.

Boore, D. M., and W. B. Joyner (1984). A note on the use of random vibration theory to predict peak amplitudes of transient signals, *Bull. Seismol. Soc. Am.* **74,** 2035–2039.

Böse, M., E. Hauksson, K. Solanki, H. Kanamori, Y. M. Wu, and T. H. Heaton (2009). A new trigger criterion for improved real-time performance of on-site earthquake early warning in southern California, *Bull. Seismol. Soc. Am.* **99,** no. 2A, 897–905.

Brown, H. M., R. M. Allen, M. Hellweg, O. Khainovski, D. Neuhauser, and A. Souf (2011). Development of the ElarmS methodology for earthquake early warning: Real time application in California and offline testing in Japan, *Soil Dynam. Earthq. Eng.* **31,** 188–200.

Brune, J. N. (1970). Tectonic stress and the spectra of seismic shear waves from earthquakes, *J. Geophys. Res.* **75,** 4997–5009.

Cartwright, D. E., and M. S. Longuet-Higgins (1956). The statistical distribution of the maxima of a random function, *Proc. Math. Phys. Sci.* **A237,** 212–232.

Clough, R. W., and J. Penzien (1975). *Dynam. Struct.* McGraw-Hill, New York, 634 pp.

Cua, G., and T. Heaton (2007). The virtual seismologist (VS) method: A Bayesian approach to earthquake early warning, in *Seismic Early Warning*, P. Gasparini, G. Manfredi, and J. Zschau (Editors), Springer, New York.

Davenport, A. G. (1964). Note on the distribution of the largest value of a random function with application to gust loading, *Proc. Inst. Civ. Eng.* **28,** 187–196.

Doi, K. (2011). The operation and performance of earthquake early warnings by the Japan Meteorological Agency, *Soil Dynam. Earthq. Eng.* **31,** 119–126.

Eisermann, A. S., A. Ziv, and G. H. Wust-Bloch (2015). Real-time back azimuth for earthquake early warning, *Bull. Seismol. Soc. Am.* **105,** no. 4, 2274–2285, doi: 10.1785/0120140298.

Eshelby, J. D. (1957). The determination of the elastic field of an ellipsoidal inclusion, and related problems, *Proc. Math. Phys. Sci.* **241,** 376–396.

Hanks, T. C., and H. Kanamori (1979). A moment magnitude scale, *J. Geophys. Res.* **84,** 2348–2350.

Hanks, T. C., and R. K. McGuire (1981). The character of high frequency strong ground motion, *Bull. Seismol. Soc. Am.* **71,** 2071–2095.

Hanks, T. C., and W. Thatcher (1972). A graphical representation of seismic source parameters, *J. Geophys. Res.* **23,** 4393–4405.

Kanamori, H. (2005). Real-time seismology and earthquake damage mitigation, *Ann. Rev. Earth Planet. Sci.* **33,** 5.1–5.20.

Kurzon, I., F. L. Vernon, A. Rosenberger, and Y. Ben-Zion (2014). Real-time automatic detectors of P and S waves using singular value decomposition, *Bull. Seismol. Soc. Am.* **104,** 1696–1708.

Lancieri, M., and A. Zollo (2008). A Bayesian approach to the real-time estimation of magnitude from the early P and S wave displacement peaks, *J. Geophys. Res.* **113,** no. B12302, 1–17.

Lancieri, M., A. Fuenzalida, S. Ruiz, and R. Madariaga (2011). Magnitude scaling of early-warning parameters for the M_w 7.8 Tocopilla, Chile, earthquake and its aftershocks, *Bull. Seismol. Soc. Am.* **101,** no. 2, 447–463.

Madariaga, R. (1976). Dynamics of an expanding circular fault, *Bull. Seismol. Soc. Am.* **65,** 163–182.

Mayeda, K., and W. R. Walter (1996). Moment, energy, stress drop, and source spectra of western United States earthquakes from regional coda envelopes, *J. Geophys. Res.* **101,** 11,195–11,208.

Nakamura, Y. (1984). Development of earthquake early-warning system for the Shinkansen, some recent earthquake engineering research and

practical in Japan, The Japanese National Committee of the International Association for Earthquake Engineering, 224–238.

Nakamura, Y. (1988). On the Urgent Earthquake Detection and Alarm System (UrEDAS), *Proc. 9th World Conference on Earthquake Engineering VII*, Tokyo, Japan, 2–9 August 1988, 673–678.

Oth, A., D. Bindi, S. Parolai, and D. Di Giacomo (2010). Earthquake scaling characteristics and the scale-(in)dependence of seismic energy-to-moment ratio: Insights from KiK-net data in Japan, *Geophys. Res. Lett.* **37,** L19304, doi: 10.1029/2010GL044572.

Sadeh, M., A. Ziv, and H. Wust-Bloch (2013). Real-time magnitude proxies for earthquake early warning in Israel, *Geophys. J. Int.* **196,** no. 2, 939–950.

Satriano, C., A. Lomax, and A. Zollo (2008). Real-time evolutionary earthquake location for seismic early warning, *Bull. Seismol. Soc. Am.* **98,** 1482–1494.

Snoke, J. A. (1987). Stable determination of (Brune) stress drops, *Bull. Seismol. Soc. Am.* **77,** 530–538.

Wu, Y. M., and H. Kanamori (2005a). Experiment on an onsite early warning method for the Taiwan early warning system, *Bull. Seismol. Soc. Am.* **95,** no. 1, 347–353.

Wu, Y. M., and H. Kanamori (2005b). Rapid assessment of damaging potential of earthquakes in Taiwan from the beginning of P waves, *Bull. Seismol. Soc. Am.* **95,** 1181–1185.

Wu, Y. M., and L. Zhao (2006). Magnitude estimation using the first three seconds P-wave amplitude in earthquake early warning, *Geophys. Res. Lett.* **33,** L16312, doi: 10.1029/2006GL026871.

Wu, Y. M., R. M. Allen, and C. F. Wu (2005). Revised M_L determination for crustal earthquakes in Taiwan, *Bull. Seismol. Soc. Am.* **95,** 2517–2524.

Ziv, A. (2014). New frequency-based real-time magnitude proxy for earthquake early warning, *Geophys. Res. Lett.* **41,** 7035–7040.

Zollo, A., G. Iannaccone, M. Lancieri, L. Cantore, V. Convertito, A. Emolo, G. Festa, F. Gallovič, M. Vassallo, C. Martino, C. Satriano, and P. Gasparini (2009). Earthquake early warning system in southern Italy: Methodologies and performance evaluation, *Geophys. Res. Lett.* **36,** L00B07, doi: 10.1029/2008GL036689.

Department of Geosciences
Tel-Aviv University
P.O. Box 39040
Tel-Aviv 6997801
Israel
itzhaklior22@gmail.com
    (I.L., A.Z.)

Laboratoire de Géologie
Ecole Normale Supérieure
24 rue Lhomond
75231 Paris cedex 05
France
    (R.M.)